Identification and paleoclimatic significance of magnetite nanoparticles in soils

Imad A. M. Ahmed[a,1] and Barbara A. Maher[b,1]

[a]Department of Earth Sciences, University of Oxford, OX1 3AN Oxford, United Kingdom; and [b]Centre for Environmental Magnetism and Palaeomagnetism, Lancaster Environment Centre, University of Lancaster, LA1 4YQ Lancaster, United Kingdom

Edited by Lisa Tauxe, University of California, San Diego, La Jolla, CA, and approved December 27, 2017 (received for review November 2, 2017)

In the world-famous sediments of the Chinese Loess Plateau, fossil soils alternate with windblown dust layers to record monsoonal variations over the last ∼3 My. The less-weathered, weakly magnetic dust layers reflect drier, colder glaciations. The fossil soils (paleosols) contain variable concentrations of nanoscale, strongly magnetic iron oxides, formed in situ during the wetter, warmer interglaciations. Mineralogical identification of the magnetic soil oxides is essential for deciphering these key paleoclimatic records. Formation of magnetite, a mixed Fe^{2+}/Fe^{3+} ferrimagnet, has been linked to soil redox oscillations, and thence to paleorainfall. An opposite hypothesis states that magnetite can only form if the soil is water saturated for significant periods in order for Fe^{3+} to be reduced to Fe^{2+}, and suggests instead the temperature-dependent formation of maghemite, an Fe^{3+}-oxide, much of which ages subsequently into hematite, typically aluminum substituted. This latter, oxidizing pathway would have been temperature, but not rainfall dependent. Here, through structural fingerprinting and scanning transmission electron microscopy and electron energy loss spectroscopy analysis, we prove that magnetite is the dominant soil-formed ferrite. Maghemite is present in lower concentrations, and shows no evidence of aluminum substitution, negating its proposed precursor role for the aluminum-substituted hematite prevalent in the paleosols. Magnetite dominance demonstrates that magnetite formation occurs in well-drained, generally oxidizing soils, and that soil wetting/drying oscillations drive the degree of soil magnetic enhancement. The magnetic variations of the Chinese Loess Plateau paleosols thus record changes in monsoonal rainfall, over timescales of millions of years.

soil magnetite | Quaternary paleoclimate | monsoon rainfall | magnetic susceptibility | structural fingerprinting

The windblown sediments of the famous Chinese Loess Plateau (CLP), spanning hundreds of meters in thickness and >600,000 km^2 in extent, potentially contain the longest, most detailed terrestrial records of East Asian monsoonal evolution. Interleaved layers of glacial-stage windblown dust (loess) and interglacial/interstadial-stage fossil soils (paleosols) span the late Pliocene and Quaternary geological periods; i.e., the last ∼3 My. Compared with the less-weathered loess layers, the interglacial paleosols contain varying but higher concentrations of nanoscale, strongly magnetic (ferrimagnetic) iron oxides, formed in situ during soil development. These variations in ferrimagnetic concentration are readily apparent even from simple room-temperature measurements of magnetic susceptibility (Fig. 1*A* and *SI Appendix*, Fig. S1). A climatic cause for the varying soil nanomagnet concentrations is evidenced by their strong correlation with the deep-sea oxygen isotope record, principally a record of continental ice volume (Fig. 1*B*).

Modern loessic soils across the Chinese Loess Plateau, and similar regions (e.g., the Russian steppe, the North American Great Plains), display a direct, strongly significant correlation of their soil-formed (pedogenic) magnetic concentrations with mean annual rainfall (1–4). This correlation, used to obtain quantified estimates of paleorainfall (5) for the Chinese monsoon region, has been linked causally to pedogenic formation of the mixed Fe^{2+}/Fe^{3+} iron oxide, magnetite, through redox changes in soil microsites following rainfall events (6–9). Electron microscopy of magnetic concentrates from the Chinese loess/paleosol sediments indicates that abiotic (extracellular) precipitation of the paleosol ferrimagnets (Fig. 1 *C* and *D*) is dominant, rather than intracellular formation of magnetosomes, of controlled size and shape, by magnetotactic bacteria (Fig. 1*E*).

Both the mineralogy of the soil ferrimagnets and their pathways of formation have been hotly debated. Opposite hypotheses link soil magnetic enhancement not with redox-related formation of the Fe^{2+}-bearing magnetite but with the formation from ferrihydrite of an oxidized, maghemite-like phase (hydromaghemite), which itself transforms to hematite upon ripening and aging (11–13). This latter pathway would thus be temperature dependent rather than moisture and redox dependent. Indeed, the transformation of ferrihydrite to maghemite has been identified in vitro (14), albeit under hydrothermal experimental conditions (150 °C for 120 d), which are environmentally unrealistic. More recently, it has been suggested that a magnetically ordered ferrihydrite, before its oxidation to hematite, might contribute to soil magnetic enhancement (15).

Magnetite has an inverse spinel structure that contains tetrahedral (T_d) and octahedral [O_h] sites accommodating Fe^{2+} and Fe^{3+} cations with a spin arrangement of $[Fe^{3+}{\downarrow}]_{T_d}[Fe^{3+}{\uparrow}Fe^{2+}{\uparrow}]_{O_h}$. Magnetite and maghemite are end members of a solid solution series. Although maghemite (γ-Fe_2O_3) has the same composition as hematite (α-Fe_2O_3), it has the structure of a spinel (a cation-deficient spinel, lacking sufficient Fe^{3+} ions to fill the available Fe sites; *SI Appendix*). Maghemite is thus ferrimagnetic, with very similar magnetic properties to magnetite. It is metastable with respect to hematite (it inverts to hematite upon heating), but can be stabilized

Significance

In the famous Chinese Loess Plateau (CLP), weakly magnetic, windblown dust layers alternate with variably magnetic fossil soils, recording monsoonal variations through the last ∼3 My. The soils contain strongly magnetic iron oxides, formed in situ, the mineralogy and paleoclimatic significance of which are controversial. Reduction of iron to form Fe^{2+}-bearing magnetite has been linked to soil wetting/drying. Conversely, oxidation of iron to form Fe^{3+}-bearing maghemite, which ages into Al-substituted hematite, has been linked to paleotemperature. This study uses structural fingerprinting and electron energy loss spectroscopy to resolve this debate, proving that magnetite is the dominant soil-formed magnet. The magnetic variations of the CLP paleosols thus record changes in monsoonal rainfall, providing a key time series for testing of general circulation climate models.

Author contributions: I.A.M.A. and B.A.M. designed research; I.A.M.A. and B.A.M. performed research; I.A.M.A. contributed new reagents/analytic tools; I.A.M.A. and B.A.M. analyzed data; and I.A.M.A. and B.A.M. wrote the paper.

The authors declare no conflict of interest.

This article is a PNAS Direct Submission.

[1]To whom correspondence may be addressed. Email: imad.ahmed@earth.ox.ac.uk or b.maher@lancaster.ac.uk.

This article contains supporting information online at www.pnas.org/lookup/suppl/doi:10.1073/pnas.1719186115/-/DCSupplemental.

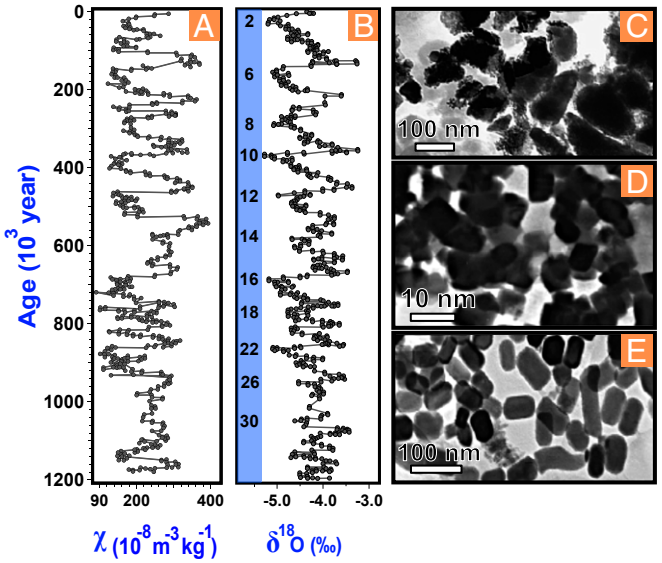

Fig. 1. (*A*) The magnetic susceptibility of the loess/paleosol sequence at Luochuan, central Chinese Loess Plateau (5); (*B*) the deep-sea oxygen isotope record from site 677 (10) (glacial stages numbered); (*C–E*) TEM micrographs of nanoscale, low-temperature ferrimagnets formed in the environment, (*C*) CLP paleosol, (*D*) United Kingdom modern cambisol (Exmoor), and (*E*) the unique crystal forms produced intracellularly by magnetotactic bacteria, Cretaceous chalk, United Kingdom.

by the presence of aluminum, one of the most commonly available metal cations in soils, substituting within some of the vacant sites.

The particle size of soil-formed ferrimagnets is magnetically distinctive, characteristically spanning the superparamagnetic (SP) to stable single domain (SSD) size range (i.e., up to ~50 nm). Curie temperature (T_c) measurements on soil and paleosol magnetic concentrates (*SI Appendix*, Fig. S3) indicate the presence in the CLP paleosols of both magnetite (T_c = 580 °C) and maghemite. However, nanoscale magnetite oxidizes at its surface to maghemite, rendering ferrite identification and quantification, whether by magnetic, X-ray diffraction, or chemical dissolution techniques, a challenging task, until now. Torrent and coauthors argue that the coexistence in soils of (trace concentrations of) ferrimagnets with (minor concentrations, up to ~5 wt%) of the highly oxidized hematite can only be explained if the ferrimagnetic phase is Fe^{3+}-bearing maghemite, not Fe^{2+}-bearing magnetite (13). They further claim that magnetite could only form if the soil is water saturated for significant periods, in order for Fe^{3+} to be reduced to Fe^{2+} (15).

Establishing the causal links between climate and soil magnetism is critically important. Past changes in the East Asian monsoon system preceded subsequent intensification of northern hemisphere glaciations (~2.8 Ma), indicating a possible leading role of monsoonal changes through switches in the poleward distribution of heat and moisture (16). The robustness of paleoclimatic reconstructions from the CLP, and their possible teleconnections, depends on identifying the composition of the abiotic ferrites in these paleosols, and hence their causal links with climatic factors. Although our understanding remains uncertain, arguably the longest and most highly resolved paleoclimate record on the continents remains underused.

To achieve unequivocal identification of the composition of soil nanomagnets, we applied structural fingerprinting from high-resolution transmission electron microscopy (HRTEM), together with energy dispersive X-ray analysis (EDXA), to soil magnetic concentrates. The structural fingerprinting approach utilizes crystallographic processing of HRTEM images in which crystal structure factors are obtained using Fourier analysis. The most probable projected crystallographic symmetries for a candidate phase are then obtained, together with geometric information (i.e., reciprocal lattice spacings and interfringe angles). The combination of geometric information on the reciprocal lattice, plane symmetry, and elemental composition (from EDXA) within a crystal leads to unambiguous identification of the nanoferrite structure.

The soil ferrites were extracted from: a modern, magnetically enhanced soil (a cambisol, from Exmoor, United Kingdom; Fig. 1*B* and ref. 17); paleosol S_1 (of last interglacial age, ~125,000 y before present [BP]) from the central region of the CLP (Luochuan; Fig. 1*A* and *SI Appendix*, Fig. S2); and a paleosol (~5 My BP) from the Mio/Pliocene red clay sequence (at Lingtai; ref. 18), which underlies the Quaternary-age loess and paleosols. To examine any possible oxidation effects related to postsampling laboratory storage, we compared recently collected (2011) and "old" (collected in 1990) samples from the Luochuan S_1 paleosol. For independent verification of our structural fingerprinting approach, we additionally used coupled scanning transmission electron microscopy and electron energy loss spectroscopy (STEM/EELS) to quantify the $Fe^{3+}/\Sigma Fe$ ratios and to identify the dominant ferrites in the "new" and long-stored Luochuan S_1 paleosol samples.

Results

Magnetic concentrates were obtained from the soil and paleosol samples; the extraction efficiency (*SI Appendix*, Table S1) quantified by before- and after-extraction measurements of magnetic susceptibility, and anhysteretic and saturation remanences (*Materials and Methods*). For each of the samples, HRTEM imaging (Fig. 2; *SI Appendix*, Fig. S10) shows agglomerated magnetic nanoparticles with dimensions ranging from ≥10 to ~50 nm and mean diameters of 19.9 × 16.2 nm (measured using a simplified elliptical geometry; *SI Appendix*, Fig. S7). Some of the larger crystals (Fig. 2*C*; *SI Appendix*, Fig. S12*A*) display euhedral, cubo-octahedral morphologies.

Critically, because reciprocal lattice geometry and plane symmetry information are diagnostic of the dominant crystal structure in the analyzed particles, it is possible to discriminate between nanocrystals of magnetite and maghemite using HRTEM (e.g., refs. 19 and 20). The *hkl* reflections (110), (210), and (321), for example, are expected for maghemite in zone axis ⟨211⟩; whereas, these reflections are forbidden in magnetite due to its crystal symmetry and *F*-centering (21, 22) (see *SI Appendix*, Figs. S9 and S10 for additional examples). Automated matching of the observed spacings and reflections against crystal standards enables analysis of statistically robust numbers (>1,000) of ferrite grains, incurring neither electron beam damage nor possible reduction artifacts, thus providing a practical, structure-sensitive probe for these pedogenic ferrites.

Applying structural fingerprinting to both the modern and fossil soil magnetic concentrates (in total to 210 HRTEM micrographs), demonstrates unequivocally that magnetite is the dominant (>75%) nanocrystalline phase in all but one sample (Fig. 3). Indeed, maghemite was found to be the dominant soil nanomagnet only in the old S_1 paleosol sample (Fig. 4 *D–F*), which had been collected and stored in the laboratory for >25 y.

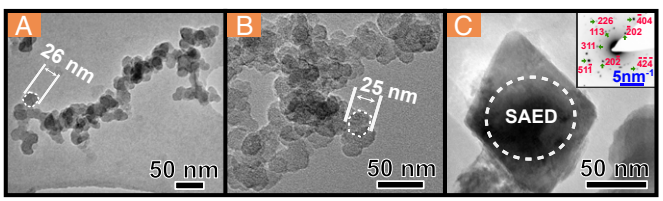

Fig. 2. (*A–C*) Magnetic concentrates from Chinese paleosols showing agglomerates of magnetic nanoparticles. The SAED of the euhedral nanoparticle in *C* identifies a magnetite structure (*Inset*) along the zone axis ⟨1$\bar{4}$1⟩.

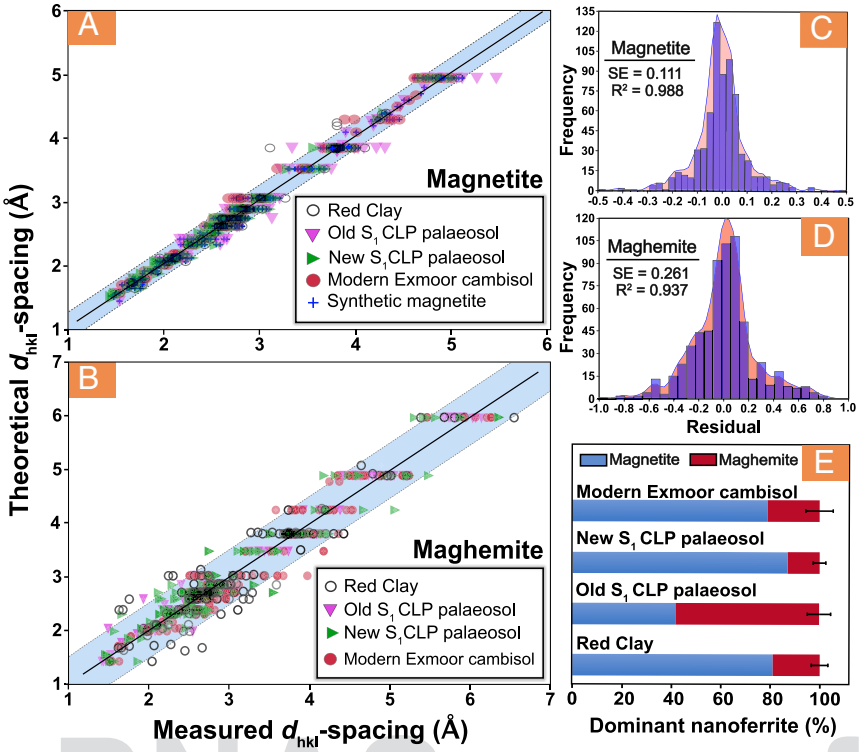

Fig. 3. Correlation plots of measured vs. theoretical interplanar distances (d_{hkl}) of (*A*) magnetite and (*B*) maghemite. The shaded areas represent the 95% prediction interval of the measured *d*-spacing and the solid line is a linear regression for the whole dataset. *C* and *D* are histogram plots of the residuals of the fits in *A* and *B* showing significant correlation for magnetite (SE estimate, SE = 0.111, R^2 = 0.988). (*E*) Magnetite and maghemite abundances in magnetic concentrates from the modern Exmoor cambisol and paleosols from the Chinese Loess Plateau, as identified by structural fingerprinting.

The HRTEM images analyzed show a mixture of aggregated/overlain ferrite grains and 3,226 recognizable single crystals. Magnetite and maghemite were the only ferrites identified by structural fingerprinting; a few (<5) two-line ferrihydrite crystals [based on the Michel et al. (23) model] were additionally identified, occurring in association with magnetite crystals in the modern Exmoor and the Pliocene red clay samples.

The possible presence of Al^{3+} ion substitution could also be examined using structural fingerprinting. Incorporation of the smaller Al^{3+} ions within the magnetite or maghemite unit cell results in modified unit cell dimensions, and accompanying alterations in lattice reflections. None of the samples displayed such modified unit cells; hence, the presence of Al^{3+} substitutions in the soil nanomagnets appears negligible. We additionally checked for Al^{3+} substitutions by elemental analysis using EDXA. The soil ferrimagnets comprise only Fe and O; they display no evidence of substitution by foreign cations (*SI Appendix*, Fig. S11).

Autocorrelation function analysis was applied to examine periodicity along a single ferrite crystal (e.g., as shown in Fig. 4) and to reveal composite (i.e., overlain) crystals. This approach can also be used to study the crystallinity of the surface layer of the magnetite particles. Areas in the HRTEM images that are dominated by amorphous carbon (from the TEM grid) or poorly crystalline clays associated with the nanoparticles give featureless autocorrelation signals (Fig. 4 *C*, 1 and 2 and *I*, 4); whereas, crystalline regions give bright continuous lines matching the orientation of the crystal. A key feature of most of the magnetite particles analyzed is the presence of an amorphous layer near their surface (e.g., compare Fig. 4 *C*, 1 with *C*, 2 and Fig. 4 *I*, 3 with *I*, 4). EDXA of this 1–4 nm thick amorphous surface layer shows no evidence of elements other than Fe, O, C, or Cu (the latter two associated with the support film and TEM grid, respectively). The autocorrelation function analysis near the magnetite surface provides no evidence of dislocations nor discontinuous coverage. These data suggest that the thin surface layer consists of maghemite, rather than clays or any sort of carbonaceous materials.

To make independent verification of our structural fingerprinting approach, we used STEM/EELS analysis to identify the ferrite mineralogy in the newer and long-stored S_1 paleosols, from Luochuan, CLP. The EELS data show distinct Fe L_2 and L_3 peaks arising from excitations of $2p_{1/2}$ and $2p_{3/2}$ core electrons to unoccupied *d*-states ($3d_{3/2}$ and $3d_{3/2}$;$3d_{5/2}$, respectively) with a consistent Fe L_3–L_2 energy difference of 13.5 ± 0.2 eV (*SI Appendix*, Fig. S12*A*). Sample spectra also show weak splitting in the Fe L_2 peaks, indicating a weak crystal field around the Fe atom (24). The spectra of the new S_1 paleosol samples show slightly wider Fe L_2 peaks (3.1–3.9 eV) compared with the old S_1 samples (3.0–3.7 eV). Weak preedge peaks at about 708 eV are visible mostly in the old S_1 samples. The calculated L_3/L_2 and the *d*-sub band occupancy H ratios (*Materials and Methods*) are 4.59–4.74 (H = 1.78–2.22) and 5.14–5.86 (H = 2.43–2.8) for the new and old paleosol samples, respectively. Assuming that the magnetic extracts contain only inverse spinel iron ferrites, a larger L_3/L_2 ratio is indicative of a higher proportion of maghemite compared with magnetite. Also, the large H ratio reflects a shift in *d*-band occupancy from the low spin (i.e., Fe^{2+}) toward the high-spin state (i.e., Fe^{3+}) as a result of magnetite oxidation. In support of these observations, the O *K*-edge data (*SI Appendix*, Fig. S12*B*) show characteristic intense prepeaks at 531 eV in the old S_1 paleosol samples, due most likely to increased Fe^{3+} concentrations. The energy difference between this prepeak and the more dominant peak at 540 eV, defined by the center of a Gaussian or a Lorentzian function fitted to the two peaks, is 9–10 eV (*SI Appendix*, Fig. S12*B*). The presence of the relatively strong peak at intensity maximum of ~547 eV in the old S_1 paleosol samples is also characteristic of a maghemite structure (25). These EELS

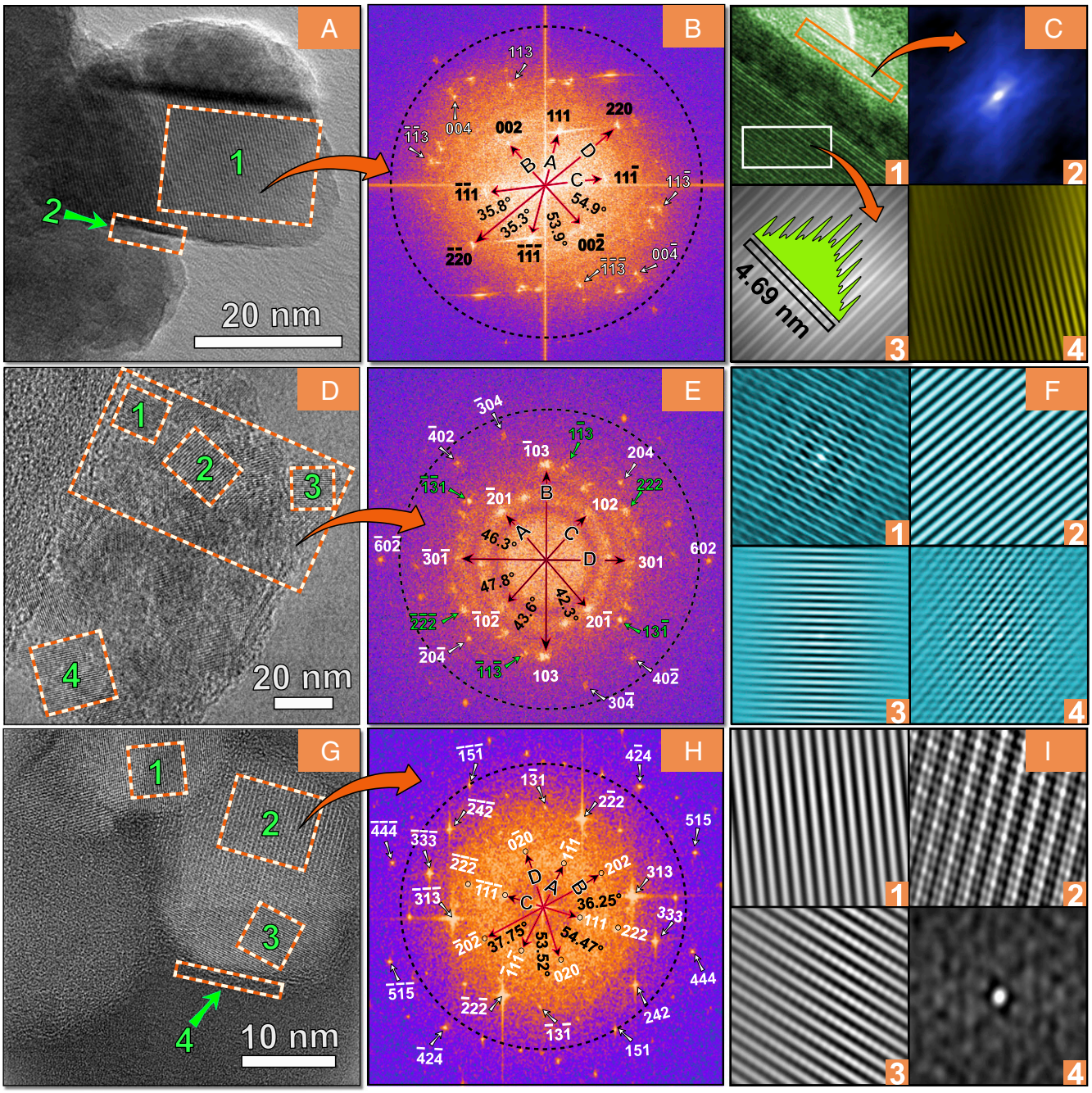

Fig. 4. HRTEM micrographs (*Left*), FFT power spectra and lattice indexing (*Middle*), and autocorrelation function analysis (*Right*). (*A*–*C*) New paleosol S_1, CLP sample, dominated by magnetite crystals (SG. $Fd\bar{3}m$): Zone axis = $\langle 1\bar{1}0 \rangle$; lattice vectors indicated by centered arrows of half lengths of $A = 2.095$, $B = 2.422$, $C = 2.069$, $D = 3.388$ nm^{-1}; *d*-spacing SD, $\sigma_d = 0.0028$; (*D*–*F*) Old paleosol S_1, CLP sample, dominated by maghemite crystals (*SG*. $P4_32_12$) with two overlying lattices: lattice 1 (lattice vectors shown): zone axis = $\langle 0\bar{1}0 \rangle$; $A = 2.614$, $B = 3.518$, $C = 2.551$, $D = 3.783$ nm^{-1}; $\sigma_d = 0.0075$; lattice 2 (lattice vectors removed for clarity; green labels): zone axis = $\langle \bar{2}11 \rangle$; $A = 3.869$, $B = 6.425$, $C = 3.668$, $D = 3.938$ nm^{-1}; $\sigma_d = 0.0107$; (*G*–*I*) Modern Exmoor sample, dominated by magnetite crystals (*SG*. $Fd\bar{3}m$): zone axis = $\langle \bar{1}01 \rangle$; $A = 1.991$, $B = 3.203$, $C = 1.968$, $D = 2.327$ nm^{-1}; $\sigma_d = 0.0042$. All Fourier transforms of the HRTEM images were indexed to satisfy the right-handed coordination system. The TEM's point resolution (kinematic diffraction ~0.625 Å^{-1}) is marked by the dotted circle on the FFT images in *B*, *E*, and *H*.

observations are thus in agreement with our structural fingerprinting analysis and provide evidence of much greater maghemitization in the old compared with the new S_1 paleosol sample.

Discussion

Our new results show that soil-formed, nanoscale ferrimagnets, extracted from magnetically enhanced soils (both modern and paleosol), are dominantly composed of discrete crystals of the mixed Fe^{2+}/Fe^{3+} iron oxide, magnetite. This definitive mineralogical identification thus demonstrates that magnetite formation occurs in well-drained, generally oxidizing soils, and substantiates the proposed causal links between the pedogenic formation of magnetite and rainfall-induced changes in soil wetness and microsite redox conditions (7, 18, 26). Conversely, the relatively small proportion of discrete maghemite nanocrystals (with the one exception of the long-stored S_1 paleosol sample) negates the

opposing hypothesis that maghemite is the major soil-formed ferrite phase. Further, there is no evidence of any substitution by Al^{3+} within these soil nanomagnets (*SI Appendix*, Fig. S11). If the proposed precursor ferrite (15) contains no Al^{3+} then it is difficult to envisage its suggested ripening and aging into an Al-substituted hematite. Finally, we find no evidence of any significant presence of magnetically ordered ferrihydrite (15).

The persistence of nanoscale magnetite particles in the paleosols, over time periods exceeding 5 My, is noteworthy. Our data indicate the presence of thin rims (1–4 nm thick) of amorphous Fe-bearing oxide material around the magnetite nanoparticles, likely an oxidized shell of maghemite. In contrast to bare synthetic magnetites, soil magnetites are always found aggregated and associated with clay minerals. Not only confined within soil micropores, the clay-coated soil magnetites thus typically encounter strong barriers to oxygen transport to their surface. Slow oxidation of the magnetite surface forms a thin maghemite rim. Mass transport through this additional protective layer becomes the rate-limiting step with increasing time. The topochemical oxidation of magnetite [Eq. **1**, after White (27)] involves the migration of Fe^{2+} ions from the core to the surface (or to the magnetite–maghemite interface) and electron exchange with dissolved oxygen at the water–mineral interface. The slow rates of solid-state outward diffusion of Fe^{2+} ions [10^{-12} – 10^{-20} cm^2/s (28–30)] and inward diffusion of protons through the magnetite–maghemite core shell is likely to be self-limiting at low soil temperature and circumneutral pH. Further liberation of core Fe^{2+} ions is expected to be hindered with increasing time as the oxidized shell becomes thicker (31). We developed an inverse shrinking-core model, based on the early work of Wen and others (32–34), to simulate the topotactic oxidation of the soil nanomagnetites. The model, which couples solid-state diffusion of Fe^{2+} (outward) and H^+ (inward) ions with oxygen gas film and chemical reaction rate-limiting controls, indicates the survival of a >20 nm magnetite core for of the order of 1–4 My (Fig. 5). This model simulation also highlights the retardation effect on magnetite oxidation as a result of increasing soil pH, with H^+ solid-state diffusion being the rate-limiting step. Dominant rainfall during the summer monsoon season (wet and warm) results in a reduction of soil pH, but this is accompanied by a sharp depletion of dissolved oxygen, thus retarding the oxidation of soil nanomagnetite. During the monsoon winter season (cold and dry), the oxygen diffusion rate increases but soil pH tends to be more alkaline due to reduced bacterial activity, resulting in at least an order of magnitude decline in the rate of magnetite oxidation.

$$3Fe^{2+}Fe_2^{3+}O_4 + \frac{1}{2}O_2 + 2H^+ \rightarrow 4\gamma - Fe_2^{3+}O_3 + Fe^{2+} + H_2O \quad [1]$$

This definitive identification of the Fe^{2+}-bearing mineral, magnetite as the dominant soil-formed ferrite phase provides a firm basis and rationale for kinetic modeling of magnetite formation processes in soil microsites under wetting and drying cycles. In turn, such modeling will enable improved quantification of East Asian paleoclimate (rainfall, evapotranspiration, temperature) over Quaternary and Mio/Pliocene timescales. Such paleoclimatic data are essential for testing and ground-truthing of general circulation models, whether for hindcasting studies or for robust prediction of future monsoon changes in the populous East Asian region.

Materials and Methods

Magnetic Extraction. Magnetic concentrates were obtained from the finer fractions (<40 μm) of the soil and paleosol samples using the extraction apparatus described in *SI Appendix*, Fig. S5. Samples were first dispersed ultrasonically and then exposed to a high-gradient magnetic extraction procedure, using a neodymium magnet (NdFeB, max. field at its tip ~40 milliTesla, mT), and under an inert (Ar) atmosphere, to preclude any oxidation of ferrites during the 14-d duration of the extraction procedure. The ferrite extraction efficiency was quantified by before- and after-extraction measurements of magnetic susceptibility, anhysteretic (peak alternating current, ac, field of 80 mT, steady direct current, dc, field 0.1 mT), and saturation remanence (peak dc field 1 T). A full description of the magnetic extraction procedure is given in the *SI Appendix*.

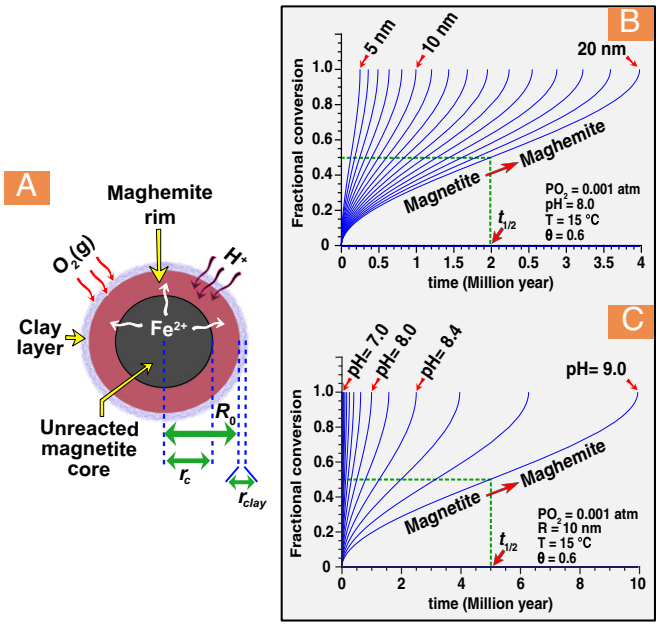

Fig. 5. Shrinking-core model simulation of the soil magnetite oxidation reaction. (*A*) Schematic representation of a reacting soil ferrite particle (initial particle radius R_0) with unreacted magnetite core (r_c), maghemite oxidation rim and an associated clay film (at t_0, $R_0 = r_c$). (*B*) Shrinking-core model simulation using P_{O_2} = 0.001 atm, T = 15 °C, air-filled porosity (θ) = 0.5, and variable R_0 between 5 and 20 nm. (*C*) Shrinking-core model simulation using R_0 = 10 nm, T = 15 °C, P_{O_2} = 0.001 atm, θ = 0.5, and variable pH between 3.0 and 9.0.

Structure Determination by HRTEM. High-resolution transmission electron microscopy was used for analysis of the soil magnetic extracts using a JEOL-3000F FEGTEM instrument operating at 300 keV. This instrument is characterized by spherical aberration coefficient of 0.57 mm and a Scherze point resolution of ~1.6 Å exceeding the (111) growth plane (d_{111} = 0.206 $Å^{-1}$) and the major characteristic lattice plane distances of the maghemite and magnetite structures. Standard synthetic Ag nanoparticles (~15 nm in diameter) and synthetic magnetite (~15–20 nm) were used for routine quality assurance and control procedures including magnification calibration for fringe spacing measurements. The lattice fringes measured for Ag (001) and magnetite (220), (311), and (440) during three different TEM sessions showed negligible drift of <0.040 Å accounting for an error of <1.5% in *d*-spacing measurements of major magnetite/maghemite reflections.

Each image was analyzed using Digital Micrograph (Gatan) and autocorrelation function analysis performed to examine periodicity information. The Fourier transform of the autocorrelation image, calculated using the fast Fourier transform (FFT) algorithm, and a structural fingerprinting approach were employed, in which lattice geometry information (i.e., the spacing of the lattice fringes and the interfringe angles) was determined. The phase of the nanocrystals in the sample was compared directly to the calculated structure factors of maghemite [*SG*. enantiomorphous pairs $P4_12_12/P4_32_12$ (35) or $P4_132/P4_332$ (35, 36)], magnetite [*SG*. $Fd\bar{3}m$ (37)] and 2L-ferrihydrite [*SG*. $P6_3mc$ (23)] phases (*SI Appendix*, Fig. S9) using SingleCrystal (CrystalMaker Software), with manual examination of all possible lattice orientations until a best fit is obtained. Where necessary, HRTEM images were denoised using the iterative Wiener filter (38). The same structure solution procedure was repeated using an iterative Matlab-based CrysTBox diffractGUI software (39). In the CrystBox diffractGUI approach, an FFT power spectrum is calculated from the input HRTEM image and Bragg reflections are detected using a Hessian or difference of Gaussian technique. The regular lattice is then extracted from thousands of possible reflections using the RANSAC (random sample consensus) algorithm; the candidate lattice with the highest score is returned defined by two vectors. The quality of the structure fingerprinting analysis was evaluated

using four output parameters: lattice check; total angular distribution; *d*-spacing STDEV (σ_d); and structure factor deviation. Each lattice candidate was also cross-checked using SingleCrystal. The fingerprinting approach was validated using three single-phase materials: Ag nanoparticles, GaN and freshly synthesized magnetite (*SI Appendix*, Fig. S8). Simulated FFT and selected area electron diffraction (SAED) of single crystal areas (e.g., Fig. 2*C*, *Inset*) were compared and found identical. This suggests that the signals from the surface and bulk structure of the analyzed samples are identical because the SAED includes information about both surface and bulk structure whereas the FFT reflects the material's surface structure.

Electron Energy Loss Spectroscopy Analysis (EELS). Samples from the new and the long-stored S_1 paleosol, from Luochuan, CLP, were additionally analyzed using EELS, with a JEOL ARM 200F TEM/STEM operating at 200 kV, equipped with a field emission gun and electron energy loss spectroscopy. STEM-EELS was acquired using a Gatan GIF Quantum ER spectrometer model 965 with a 2.5-mm spectrometer entrance aperture. The camera length was chosen so that Quantum gives a collection half-angle of 38.19 mrad, resulting in high collection efficiency and initial energy resolution of ~1.0 eV (0.1 eV/channel dispersion) determined by measuring the full width at half maximum of the zero-loss peak (ZLP). The exposure time of each EELS spectrum was set to ≤10 s to avoid radiation damage. All datasets were energy calibrated by aligning the maximum of the ZLP of each EELS spectrum to the same channel. The core-loss EELS spectra were constructed using a curve fitting approach described by ref. 40. The model consisted of a power-law background, Fe $L_{2,3}$ and O *K*-edges and their fine structures, multiple scattering, and Hartree–Slater cross-section components. The model was fitted using the Levenberg–Marquardt method and used to determine the *d*-band occupancy the relative intensity of the white lines (L_3/L_2) (or the branching ratio $Q = I(L_3)/[I(L_2) + I(L_3)]$), which was shown to characterize iron oxides (40, 41). A ratio, termed here as H-ratio, developed by Colliex et al. (40) and Morrison et al. (42) is also used here to characterize the occupancy of the *d*-states. The H ratio is sensitive to increases in populations of higher oxidation states of an ion in the *3d* orbital and is defined as: $H = h_{d_{5/2}}/h_{d_{3/2}} = 1/6[5/2I_{L_3}/I_{L_2}E_{L_2}/E_{L_3} - 1]$, where E_{L_2} and E_{L_3} are the energies of the L_2 and L_3 peaks determined by fitting Gaussian or Lorentzian function and the determination of the center of the L_2 and L_3 peaks.

ACKNOWLEDGMENTS. We thank Kerstin Jurkschat and Ian Griffiths for help in TEM imaging and EELS analysis, Vassil Karloukovski for assistance with magnetic measurements, and Tom Stevens and Sim Spassov, for kindly providing "new" samples of the Luochuan S_1 paleosol, and the Lingtai Red Clay sample, respectively. We also thank Miloslav Klinger for providing access to the CrystBox package and for the helpful discussion. We thank the Oxford Materials Characterisation Service for providing access to HRTEM facilities.

1. Maher BA, Thompson R (1995) Paleorainfall reconstructions from pedogenic magnetic susceptibility variations in the Chinese Loess and Paleosols. *Quat Res* 44:383–391.
2. Maher BA, Alekseev A, Alekseeva T (2002) Variation of soil magnetism across the Russian steppe: Its significance for use of soil magnetism as a palaeorainfall proxy. *Quat Res* 21:1571–1576.
3. Geiss CE, Zanner CW (2007) Sediment magnetic signature of climate in modern loessic soils from the Great Plains. *Quat Int* 162–163:97–110.
4. Song Y, et al. (2014) Quantitative relationships between magnetic enhancement of modern soils and climatic variables over the Chinese Loess Plateau. *Quat Int* 334–335: 119–131.
5. Maher BA, Possolo A (2013) Statistical models for use of palaeosol magnetic properties as proxies of palaeorainfall. *Glob Planet Change* 111:280–287.
6. Maher BA, Thompson R (1999) Palaeomonsoons I: The magnetic record of palaeoclimate in the terrestrial loess and palaeosol sequences. *Quaternary Climates, Environments and Magnetism*, eds Maher BA, Thompson R (Cambridge Univ Press, Cambridge, UK), pp 81–125.
7. Maher BA, Thompson R (1992) Paleoclimatic significance of the mineral magnetic record of the Chinese loess and paleosols. *Quat Res* 37:155–170.
8. Maher BA, Taylor RM (1988) Formation of ultrafine-grained magnetite in soils. *Nature* 336:368–370.
9. Orgeira MJ, Egli R, Compagnucci RH (2011) A quantitative model of magnetic enhancement in loessic soils. *The Earth's Magnetic Interior* (Springer, Dordrecht, The Netherlands), pp 361–397.
10. Raymo ME, Ruddiman WF, Shackleton NJ, Oppo DW (1990) Evolution of Atlantic Pacific delta-C-13 gradients over the last 2.5 My. *Earth Planet Sci Lett* 97:353–368.
11. Barrón V, Torrent J, De Grave E (2003) Hydromaghemite, an intermediate in the hydrothermal transformation of 2-line ferrihydrite into hematite. *Am Mineral* 88: 1679–1688.
12. Torrent J, Barrón V, Liu Q (2006) Magnetic enhancement is linked to and precedes hematite formation in aerobic soil. *Geophys Res Lett* 33:L02401.
13. Torrent J, Liu Q, Bloemendal J, Barrón V (2007) Magnetic enhancement and iron oxides in the upper luochuan Loess-paleosol sequence, Chinese Loess plateau. *Soil Sci Soc Am J* 71:1570–1578.
14. Liu Q, Barrón V, Torrent J, Eeckhout SG, Deng C (2008) Magnetism of intermediate hydromaghemite in the transformation of 2-line ferrihydrite into hematite and its paleoenvironmental implications. *J Geophys Res* 113:B01103.
15. Michel FM, et al. (2010) Ordered ferrimagnetic form of ferrihydrite reveals links among structure, composition, and magnetism. *Proc Natl Acad Sci USA* 107: 2787–2792.
16. Maher BA (2016) Palaeoclimatic records of the loess/palaeosol sequences of the Chinese Loess Plateau. *Quat Sci Rev* 154:23–84.
17. Maher BA (1998) Magnetic properties of modern soil and Quaternary loessic paleosols. Paleoclimatic implications. *Palaeogeogr Palaeoclimatol Palaeoecol* 137:25–54.
18. Maher BA, Alekseev A, Alekseeva T (2003) Magnetic mineralogy of soils across the Russian Steppe: Climatic dependence of pedogenic magnetite formation. *Palaeogeogr Palaeoclimatol Palaeoecol* 201:321–341.
19. Moeck P, Fraundorf P (2007) Structural fingerprinting in the transmission electron microscope: Overview and opportunities to implement enhanced strategies for nanocrystal identification. *Zeitschrift für Kristallographie* 222:634–645.
20. Peter M, Bjorge R (2011) Lattice-fringe fingerprinting: Structural identification of nanocrystals by HRTEM. *MRS Proc*, 10.1557/PROC-1026-C17-10.
21. Fleet ME (1986) The structure of magnetite: Symmetry of cubic spinels. *J Solid State Chem* 62:75–82.
22. Collyer S, Grimes NW, Vaughan DJ (2000) Does magnetite lack a centre of symmetry? *J Phys C Solid State Phys* 21:L989–L992.
23. Michel FM, et al. (2007) The structure of ferrihydrite, a nanocrystalline material. *Science* 316:1726–1729.
24. Chen S-Y, et al. (2009) Electron energy loss spectroscopy and ab initioinvestigation of iron oxide nanomaterials grown by a hydrothermal process. *Phys Rev B* 79:104103.
25. Golla-Schindler U, Hinrichs R, Bomati-Miguel O, Putnis A (2006) Determination of the oxidation state for iron oxide minerals by energy-filtering TEM. *Micron* 37:473–477.
26. Le Borgne E (1955) Susceptibilité magnétique anormale du sol superficiel [Abnormal magnetic susceptibility of surface soil]. *Ann Geophys* 11:399–419.
27. White AF (1990) Heterogeneous electrochemical reactions associated with oxidation of ferrous oxide and silicate surfaces. *Mineral-Water Interface Geochemistry* (Mineral Society of America, Washington, DC).
28. Sidhu PS, Gilkes RJ, Posner AM (1977) Mechanism of low-temperature oxidation of synthetic magnetites. *J Inorg Nucl Chem* 39:1953–1958.
29. White AF, Peterson ML, Hochella MF (1994) Electrochemistry and dissolution kinetics of magnetite and ilmenite. *Geochim Cosmochim Acta* 58:1859–1875.
30. Tang J, Myers M, Bosnick KA, Brus LE (2003) Magnetite Fe_3O_4 nanocrystals: Spectroscopic observation of aqueous oxidation kinetics. *J Phys Chem B* 107:7501–7506.
31. Ge K, Williams W, Liu Q, Yu Y (2014) Effects of the core-shell structure on the magnetic properties of partially oxidized magnetite grains: Experimental and micromagnetic investigations. *Geochem Geophys Geosyst* 15:2021–2038.
32. Wen CY (1968) Noncatalytic heterogeneous solid-fluid reaction models. *Ind Eng Chem* 60:34–54.
33. Yagi S, Kunii D (1961) Fluidized-solids reactors with continuous solids feed—I residence time of particles in fluidized beds. *Chem Eng Sci* 16:364–371.
34. Levenspiel O (1999) *Chemical Reaction Engineering* (Wiley, New York).
35. Greaves GN (1983) A powder neutron diffraction investigation of vacancy ordering and covalence in γ-Fe_2O_3. *J Solid State Chem* 49:325–333.
36. Pecharroman C, Gonzalezcarreno T, Iglesias JE (1995) The infrared dielectric-properties of maghemite, γ-Fe_2O_3, from reflectance measurement on pressed powders. *Phys Chem Miner* 22:21–29.
37. Fleet ME (1981) The structure of magnetite. *Acta Crystallogr B* 37:917–920.
38. Kilaas R (1998) Optimal and near-optimal filters in high-resolution electron microscopy. *Microscopy (Oxf)* 190:45–51.
39. Klinger M, Polívka L, Jäger A, Tyunina M (2016) Quantitative analysis of structural inhomogeneity in nanomaterials using transmission electron microscopy. *J Appl Crystallogr* 49:762–770.
40. Colliex C, Manoubi T, Ortiz C (1991) Electron-energy-loss-spectroscopy near-edge fine structures in the iron-oxygen system. *Phys Rev B Condens Matter* 44:11402–11411.
41. Taftø J, Krivanek OL (1982) Site-specific valence determination by electron energy-loss spectroscopy. *Phys Rev Lett* 48:560–563.
42. Morrison TI, Brodsky MB, Zaluzec NJ (1987) EELS as a probe of d-band occupancy in magnetic-alloys. *Ultramicroscopy* 22:125–127.

PNAS
Proceedings of the National Academy of Sciences of the United States of America www.pnas.org

Supporting Information Appendix for

The identification and paleoclimatic significance of magnetite nanoparticles in soils

Imad A.M. Ahmed[1] and Barbara A. Maher[2*]

[1]Department of Earth Sciences, University of Oxford, South Parks Road, Oxford OX1 3AN, UK.

[2]Centre for Environmental Magnetism and Palaeomagnetism, Lancaster Environment Centre, University of Lancaster, Lancaster, LA1 4YQ, UK.

This PDF file includes:

- **Supplementary Text**
  - *Soil and paleosol samples*
  - *Magnetic Extraction*
  - *Crystal structure of magnetite and maghemite*
  - *Ferrite particle size distribution*
  - *Examples of structural 'fingerprinting' analysis applied to pedogenic ferrites.*
- Table S1: Magnetic properties of the soil and paleosol samples (< 40 µm), pre- and post-magnetic extraction.
- Fig. S1: The sediment sequences, and magnetic susceptibility logs, from west to east and south in the Chinese Loess Plateau
- Fig. S2: Map of the Chinese Loess Plateau, showing the location of the Luochuan and Lingtai sequences
- Fig. S3: Magnetisation versus temperature for paleosol S_5 from Luochuan, CLP
- Fig. S4: X-ray (Co-K_α) diffractograms for the bulk soil and paleosol samples
- Fig. S5: Schematic drawing of the experimental set-up used for the magnetic extraction procedure from soil and paleosol samples.
- Fig. S6: Crystal structure and spin configuration of magnetite and maghemite
- Fig. S7: Particle size distribution of magnetic nanoparticles from the soil and paleosol samples listed in Table S1.
- Fig. S8: Structural 'fingerprinting' of: single phase GaN crystal, Ag nanoparticles and synthetic magnetite
- Fig. S9: Electron diffraction from ideal maghemite, magnetite and 2L-ferrihydrite structures
- Fig. S10: Examples demonstrating the application of the structural 'fingerprinting' approach
- Fig. S11: Energy-dispersive x-ray spectroscopy analysis (EDXA) data and HRTEM from magnetic extracts.
- Fig. S12: EELS spectra of paleosol magnetic nanoparticles

Supplementary Text

Soil and paleosol samples

Fig. S1 illustrates the interleaved stratigraphy of the less-weathered loess layers and variably-developed paleosols across the Chinese Loess Plateau (CLP), together with their magnetic susceptibility variations, from the more arid, high sedimentation rate sites in the west to the increasingly humid, lower sedimentation rate sites in the east and south. For this study, we analysed samples from one modern soil, a magnetically-enhanced cambisol developed on a non-magnetic parent material (slate), from Exmoor, U.K., and from paleosols from the Chinese Loess Plateau (CLP). The latter comprised: samples from the last-interglacial paleosol, S_1 (~125 kyrs age), from Luochuan, in the central region of the CLP; and a sample ~ 5 million years in age (from Lingtai), from the Red Clay, the Mio/Pliocene paleosol sequence which underlies the Quaternary-age loess/paleosol sediments. The locations of the Lingtai (35.0°N, 107.5°E) and classic Luochuan (35.8°N, 109.4°E) sections in the central Loess Plateau are shown in Fig. S2. The Luochuan section is ~135 m thick, and comprises more than 30 loess–paleosol alternations, spanning all of the Quaternary period. The Lingtai sequence consists of ~130 m of Red Clay, of late Miocene/Pliocene age, overlain by ~170 m of interbedded Quaternary loess and paleosols. We analysed both recently-collected (2011) S_1 samples from Luochuan (kindly provided by Tom Stevens), and samples collected in 1990 (by B. Maher), and subsequently stored in the laboratory. Magnetic and XRD data have previously been reported for the Exmoor modern soil and the Luochuan paleosols (1), and Fig. S3 and Fig. S4. Thermomagnetic analysis of CLP paleosols typically indicates the presence of both magnetite and maghemite (Fig. S3). The majority of the sample magnetisation is lost at ~ 580 °C, the Curie point of magnetite. The inflections in the heating curve at ~300 - 500 °C occur as maghemite (especially the finest-grained particles)

oxidises to hematite. This maghemite-hematite conversion is reflected in the loss of magnetisation (marked by the thick arrow on the y-axis) seen in the cooling curve.

In terms of mineralogy, the bulk soil samples are dominated (~89 wt%) by quartz, clay minerals (including chlorite and illite), and trace (~0.42 wt%) indications of the presence of magnetite and/or maghemite (Fig. S4). Magnetite and maghemite are ferrimagnetic; they have strong positive exchange interactions between their neighbouring atomic magnetic moments, and unequal Fe occupancy in the octahedral and tetrahedral sites, resulting in spontaneous magnetisations and large induced magnetisations, which resist thermal disturbance. Even though these minerals occur in soils typically in trace concentrations (e.g., up to 0.3 % in the CLP paleosols), they account for > 90% of the measured magnetic remanence. In contrast, the weakly-magnetic iron minerals, hematite and goethite, typically occur in minor concentrations (up to ~5%) but contribute very little to soil magnetic susceptibility, anhysteretic remanence (ARM) or saturation isothermal remanent magnetisation (SIRM).

Magnetic Extraction

The soil and paleosol samples were subjected to a magnetic extraction procedure using a modified approach based on Petersen *et al*. (2) and Hounslow *et al*. (3, 4). The new modification aimed to protect the ultrafine ferrite particles from oxidation or structural alterations during the magnetic extraction. Briefly, ~1.0 g of dry soil sample was moved to an Ar glovebox and ground gently with an agate pestle and mortar; excessive or forceful grinding that may lead to breaking detrital magnetite particles was avoided. The sample was then dispersed in 50 ml oxygen-free MilliQ water (O_2 < 0.1 ppm) containing 0.20 g sodium hexametaphosphate inside the Ar glovebox. The sample was mixed by shaking for 5 min and subjected to ultrasonication for 2 min.

The >40 μm fraction was separated from the fine fraction by centrifugation (2000 rpm for 1.5 min). The above procedure was repeated 10-15 times.

The separated < 40 μm soil fraction was then circulated around a magnetic extraction apparatus (Fig. S5) using a peristaltic pump. In this apparatus, an NdFeB (560 milliTesla, mT) magnet is placed on top of a PTFE-coated stainless-steel needle, generating a high-gradient magnetic field (max ~40 mT) around its tip. The magnetic extraction was carried out for 14 days under continuous flow of Ar gas. The magnetic extracts accumulated near the tip of the needle were collected once a day by closing the flushing gate and rinsing the needle with deoxygenated MilliQ water through the rinsing port (Fig. S5). The collected magnetic extracts were transferred immediately to the Ar-glovebox and stored until analysed.

In order to quantify the efficiency of the magnetic extraction procedures, we made before- and after-extraction measurements of magnetic susceptibility, and room-temperature anhysteretic (peak alternating current, ac, field of 80 mT, steady direct current, dc, field 0.1 mT) and saturation remanence (peak dc field 1 T). The magnetic measurements were made at the Centre for Environmental Magnetism and Paleomagnetism, Lancaster University. Room-temperature remanent magnetisations (IRMs) were measured with a Molspin minispin magnetometer (mean background noise level 0.1 x 10^{-8} A m^2). To identify magnetic grain sizes and/or magnetic interactions (5, 6), anhysteretic remanence (ARM) was induced in a decaying (80 mT, peak) alternating magnetic field (AF), with a small superimposed direct current (DC) field (0.01 mT), and subsequently AF-demagnetized. Stepwise remanence acquisition was measured with incremental application of DC fields of 10, 20, 30, 50, 75, 100, and 300 mT and 1 T. The extraction efficiency data for each of the three measured magnetic parameters (Table S1) show

that the extraction process removed significant proportions of the susceptibility and remanence carriers in each of the analysed soil and paleosol samples.

Crystal structure of magnetite and maghemite

Magnetite (Fe_3O_4) and maghemite (γ-Fe_2O_3) are ferrimagnetic at room temperature. Both materials crystallise in a similar close-packed cubic lattice rendering them indistinguishable by standard resolution x-ray diffraction. The key structural differences between magnetite and maghemite lie in the properties of the tetrahedral and octahedral sites.

Magnetite is a mixed Fe^{2+}/Fe^{3+} inverse spinel phase with a typical cubic lattice system in which A-sites (tetrahedral with spin down) are occupied by only Fe^{3+} cations whereas B-sites (octahedral with spin up) contain equal numbers of Fe^{2+} and Fe^{3+} cations (Fig. S6). The inverse spinel structure of magnetite can be described as $(Fe^{3+})_8^{tetra}\left[Fe_{\frac{1}{2}}^{3+}Fe_{\frac{1}{2}}^{2+}\right]_{16}^{octa}O_{32}$, where *tetra* and *octa* denote the tetrahedrally and octahedrally coordinated sites, respectively, of the $Fd\bar{3}m; (a = 8.394\ \text{Å})$ space group. Mössbauer studies of cubic-phase magnetite have shown that at room temperature iron atoms on the B-site behave like $Fe^{2.5+}$ due to electron hopping between the Fe^{2+} and Fe^{3+} sites of the mixed valance octahedral site giving rise to electrical conductivity and a magnetic moment of 4 Bohr magneton (μ_B) per Fe_3O_4 formula unit (7-10).

Magnetite is stoichiometric (i.e., $\frac{Fe_A}{Fe_B} = 0.5$) when the moles of vacancies δ = 0 and non-stoichiometric when $0 < \delta < \frac{1}{3}$. When the extreme condition $\delta = \frac{1}{3}$ is reached, the structure becomes depleted in Fe^{2+} and maghemite is formed. The general maghemite cubic-phase

structure can be derived from magnetite by introducing $\frac{8}{3}$ vacancies in the B-site; oxidation of magnetite into maghemite can be schematised as follows:

$$(Fe^{3+})_8^{tetra}\left[Fe_{\frac{1}{2}}^{3+}Fe_{\frac{1}{2}}^{2+}\right]_{16}^{octa}O_{32} \rightarrow (Fe^{3+})_8^{tetra}\left[Fe_{\frac{5}{6}}^{3+}\square_{\frac{1}{6}}\right]_{16}^{octa}O_{32}$$

magnetite *maghemite*

Early studies (e.g., (11, 12)) suggested randomly distributed cation vacancies over the octahedral sites in maghemite, with an assumed cubic space group of *Fd3m*. However, there is increasing evidence that ageing of soil maghemite leads to ordering of the vacancies, giving rise to superstructure lines (similar to $LiFe_5O_8$ (13)) in the x-ray diffraction pattern, and reduces the maghemite cell symmetry to tetragonal space group ($P4_32_12$/ $P4_12_12$; a = 8.322 Å, c = 24.996-25.113 Å) by tripling its basic cubic unit cell along the *c*-axis (14-16). The tetragonal spinel structures of maghemite are most common in synthetic and natural samples although some limited reports have identified primitive cubic maghemite (i.e., $P4_332$/$P4_132$) in some rock specimens (17, 18). This departure of maghemite from the cubic *Fd3m* symmetry towards the more ordered tetragonal or primitive cubic symmetry in soils allows the elucidation of the ferrite structure using the integrative structural fingerprinting approach described here.

Ferrite particle size distribution

The diameters of the ferrite particles were derived by image analysis of >200 HRTEM micrographs (N = 3090 individual ferrite crystals) using ImageJ (19) assuming (for measurement purposes) an elliptical geometry for each single grain (Fig. S7). For the major axis distribution, Q_{1x} = 12.61 nm, Q_{2x} = 22.4 nm, μ_x= 19.9 nm and for the minor axis distribution Q_{1y} = 10.7 nm, Q_{2y} = 17.9 nm, μ_y= 16.2 nm, where Q_1 and Q_2 are the first and second quartiles and μ is the

mean. The particle size distribution indicates that ~25% of the ferrimagnetic particles fall within the superparmagnetic (SP) size range whereas the remaining 75% of the population fall within the stable single domain fraction (SSD) size range. Viscous superparamagnetic particles (VSP) that would saturate in relatively low magnetic fields, and show time- and frequency-dependent magnetic behaviour, are located at the SP-SSD interface (Fig. S7).

Examples of structural 'fingerprinting' analysis applied to pedogenic ferrites.

Idealised electron diffraction reflections presented in Fig. S9 of tetragonal maghemite ($P4_32_12$; c=25.113 Å (14) *and* c =8.322 Å (20)), primitive cubic maghemite ($P4_132$; c=8.330 Å(21)), magnetite ($Fd\bar{3}m$; c=8.394 Å (22) and 2L-ferrihydrite ($P6_3mc$ (23)) demonstrate structural differences between these candidate phases in soil magnetic extracts. The data presented in Fig. S10 provide four examples of structural 'fingerprinting' analysis, as applied to the soil and paleosol samples analysed here. In the first example ('old' S_1, Luochuan, CLP paleosol, (a) – (e)), primitive cubic maghemite ($P4_132$; c = 8.330 Å) is found to provide the best fit of the regular lattice of multiple grains (b) along zone-axis $\langle\bar{2}51\rangle$ (A = 3.834, B = 5.635, C =3.797, D = 5.146 nm^{-1}; d-spacing STDEV = 0.0013, total angular distribution = 3.61). Together with the good fit statistics to the maghemite structure, these data (620 particles analysed) demonstrate that the dominant ferrite phase in this long-stored CLP S_1 sample is cubic maghemite. In the second example, from the 'new' S_1, Luochuan paleosol (Fig. S9 (f) – (j)), magnetite provides the best fit to the magnetic lattice along the zone axis $\langle1\bar{1}1\rangle$ with (A = 3.410, B = 3.450, C =3.408, D = 5.881 nm^{-1}; σ_d = 0.0020, total angular distribution = 3.19. If maghemite is the dominant phase then it would be expected to find any of the strong reflections (110), (101), ($1\bar{1}2$) or their symmetry equivalent reflections but all these reflections were absent. In addition, the maghemite

fits ($P4_32_12$ or $P4_132$) produced large *d*-spacing STDEV (0.0089 - 0.0193) and total angular distribution (30.8 -113.11), hence identifying that these crystals are magnetites. In the third example, from the modern Exmoor cambisol (Fig. S10 (k) – (l)), both magnetite and maghemite provided reasonable fit to the structure but the optimal zone axes found allow the differentiation between the two phases based on missing or forbidden reflections. In this case, magnetite provided the best goodness of fit (STDEV and total angular distribution) and hence these crystals are magnetites. Magnetite zone-axis $\langle 1\bar{1}2\rangle$: A = 3.447, B = 3.941, C = 2.074, D = 4.103 nm^{-1}, d-spacing STDEV = 0.0039, total angular distribution = 12.83. Maghemite ($P4_32_12$) zone-axis $\langle\bar{1}01\rangle$: A = 3.941, B = 4.480, C = 2.112, D = 4.462 nm^{-1}, d-spacing STDEV = 0.00116, total angular distribution = 224.30. In the fourth example, from the Lingtai Red clay (Fig. S10 (m) – (n)), magnetite provides the best fit to the structure of a single crystallite along the zone-axes $\langle\bar{1}01\rangle$ (A = 3.645, B = 3.801, C =3.148, D = 5.651 nm^{-1}; σ_d = 0.0042). The absence of the 0.170 $Å^{-1}$ reflections (forbidden in magnetite) from the (110), (101) and mirror planes and the presence of strong reflection of the (202) (see Fig. S9) suggests that magnetite is the correct ferrite phase and not any of the maghemite structures or the 2L-ferrihydrite.

Table S1. Magnetic properties of the soil and paleosol samples (< 40 μm), pre- and post-magnetic extraction.

Sample	χ_{pre}	χ_{post}	χ % ext. eff.	ARM_{pre}	ARM_{post}	ARM % ext. eff.	$SIRM_{pre}$	$SIRM_{post}$	SIRM % ext. eff.
PSBE, Exmoor cambisol, Pinkery Farm (20 cm)	26.4	9.9	62	2.0	1.5	21	1.0	0.6	44
'OLD' CLP1 Luochuan paleosol, (collected 1990)	231.5	112.75	52	106.2	55.9	48	12.25	7.8	37
'NEW' CLP1 S_1, Luochuan paleosol, 9.1 m depth (collected in 2011)	326.8	125	62	126.1	59.25	53	14.95	8.75	42
RED CLAY Tertiary Red Clay, Lingtai, 260.94 m, 5.36 Myrs BP	140.0	96.3	31	100.2	70.4	30	9.0	7.0	23

χ = mass-specific magnetic susceptibility (10^{-8} m^3 kg^{-1}); ARM = mass-specific anhysteretic remanent magnetisation (10^{-5} Am^2 kg^{-1}); SIRM = mass-specific saturation isothermal remanent magnetisation (10^{-3} Am^2 kg^{-1}).

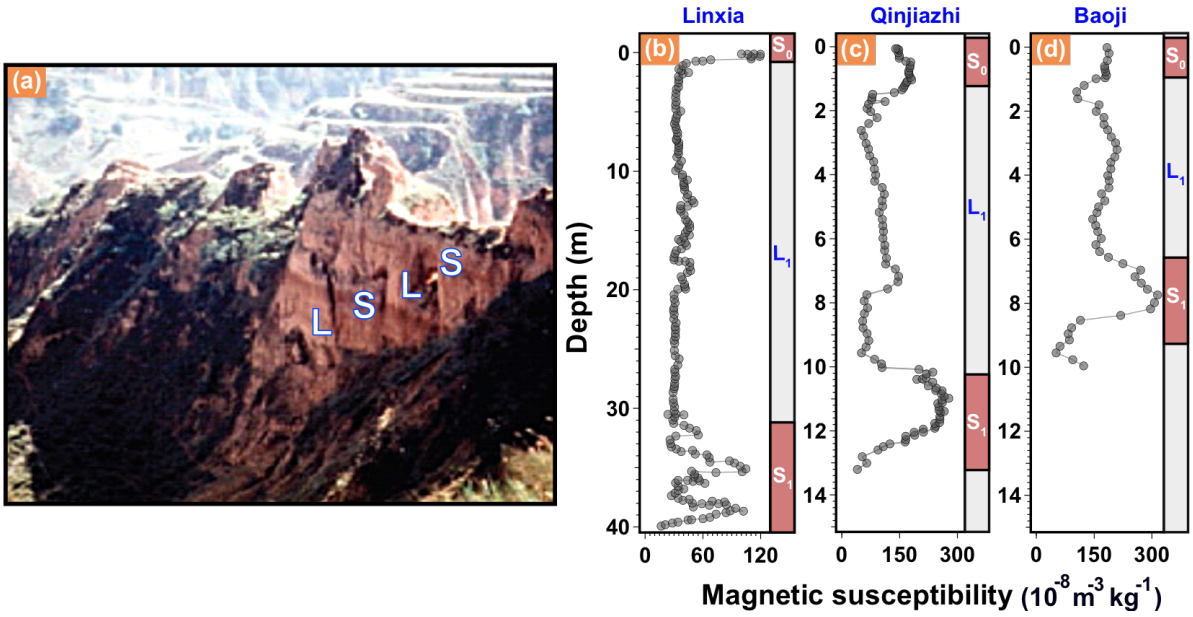

Fig. S1. (a) The sediment sequence in the central Chinese Loess Plateau, showing the reddened paleosols (S) interbedded with the lighter-coloured parent loess (L, windblown dust), and (b – d) the varying degrees of magnetic enhancement in the paleosols, lowest in the driest and highest-sedimentation rate sites in the west (b), and increasingly high in the wetter and lower-sedimentation sites to the east (c) and south (d). S_0 = present interglacial soil; L_1 = last-glacial windblown loess; S_1 = last interglacial soil. Sample locations are shown in SI Appendix Fig. S2. Reprinted from ref. 25, with permission from Elsevier.

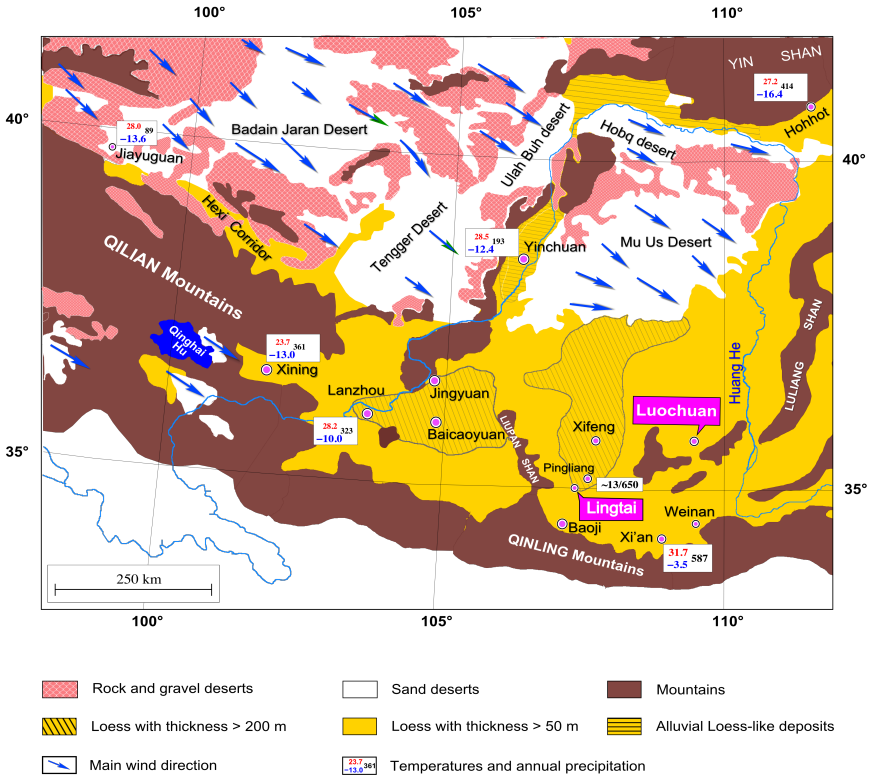

Fig. S2. Map of the Chinese Loess Plateau, showing the location of the Luochuan and Lingtai sequences. Adapted from Spassov (2002) (24) and reprinted from ref. 25, with permission from Elsevier.

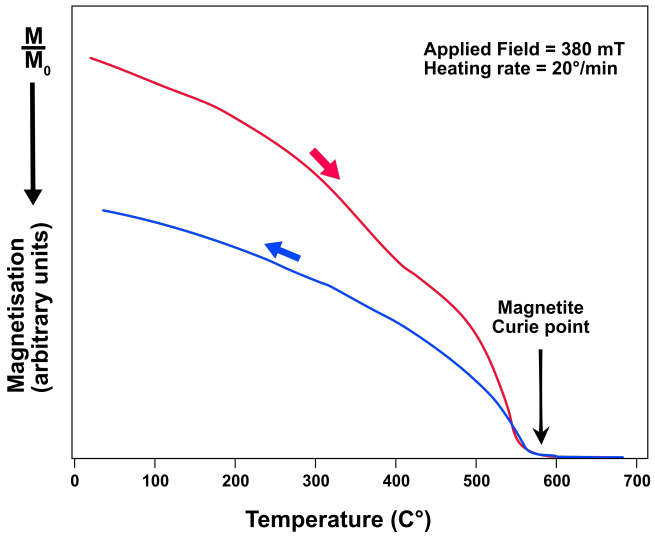

Fig. S3. Magnetisation versus temperature for paleosol S_5 from Luochuan, CLP (magnetic susceptibility = 256×10^{-8} m^3 kg^{-1}). Reprinted from ref. 25, with permission from Elsevier.

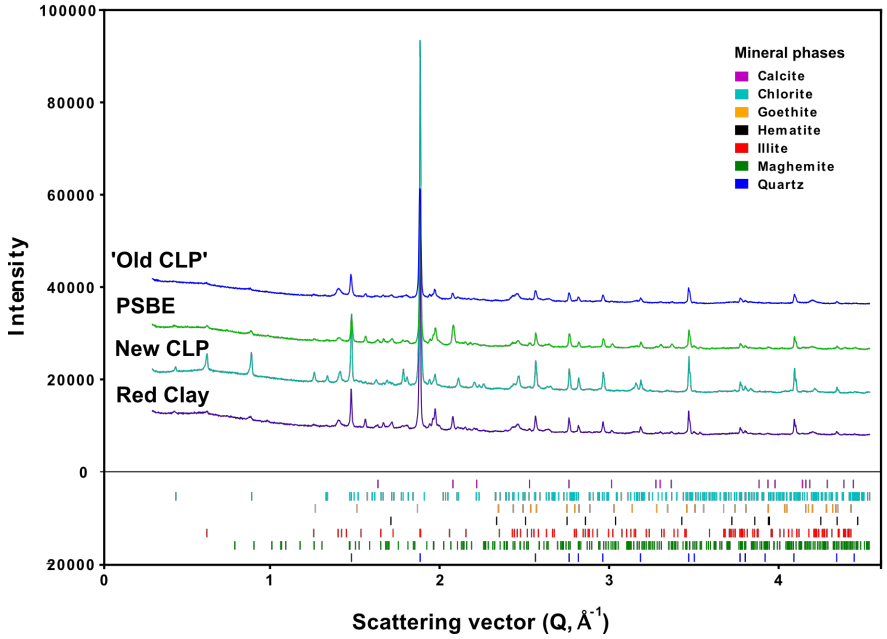

Fig. S4. X-ray (Co-K_α) diffractograms for the bulk soil and paleosol samples. The samples are dominated by quartz, illite, Fe-chlorite, hematite, goethite, calcite and magnetite/maghemite with average compositions (based on semi-quantitative XRD analysis) of 51.25%, 26.08%, 11.8%, 2.78%, 6.86%, 0.81% and 0.42%, respectively.

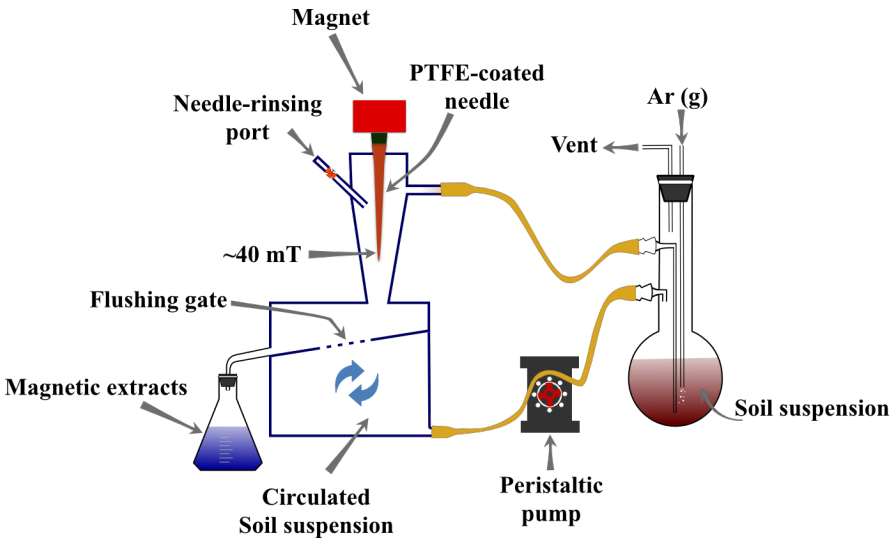

Fig. S5. Schematic drawing (not to scale) of the experimental set-up used for the magnetic extraction procedure from soil and paleosol samples.

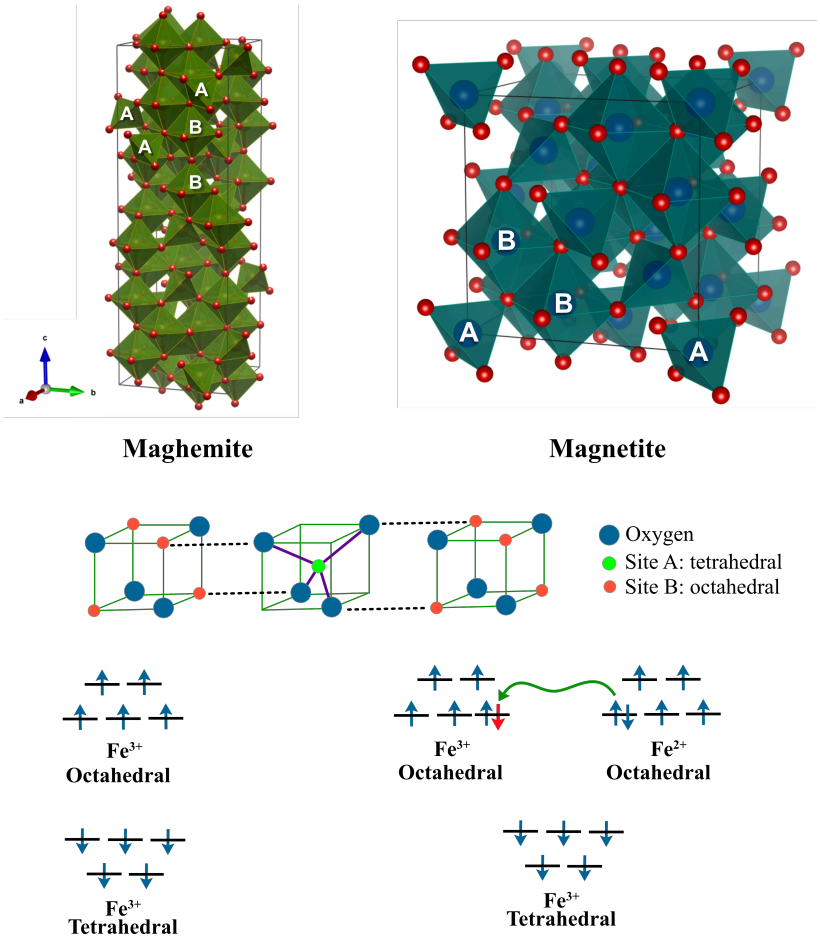

Fig. S6. Crystal structure and spin configuration of magnetite ($Fd\bar{3}m; a = 8.394$ Å) and maghemite ($P4_32_12; a = 8.322$ Å; $c = 25.113$ Å).

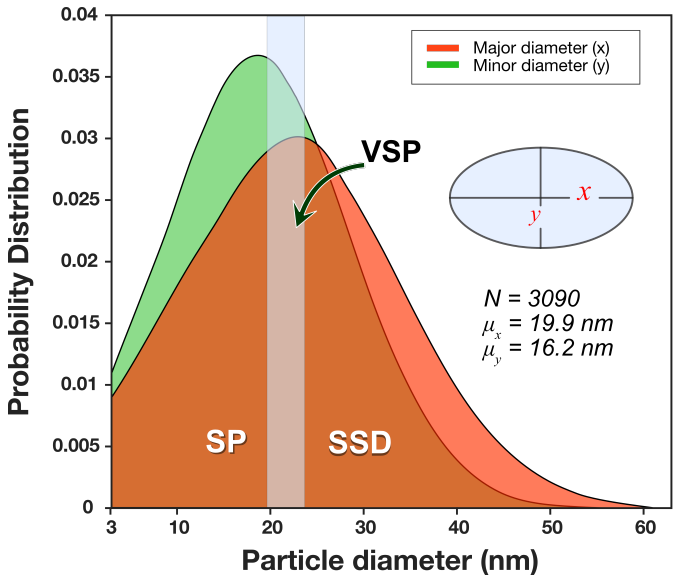

Fig. S7. Particle size distribution of magnetic nanoparticles from the soil and paleosol samples listed in Table S1.

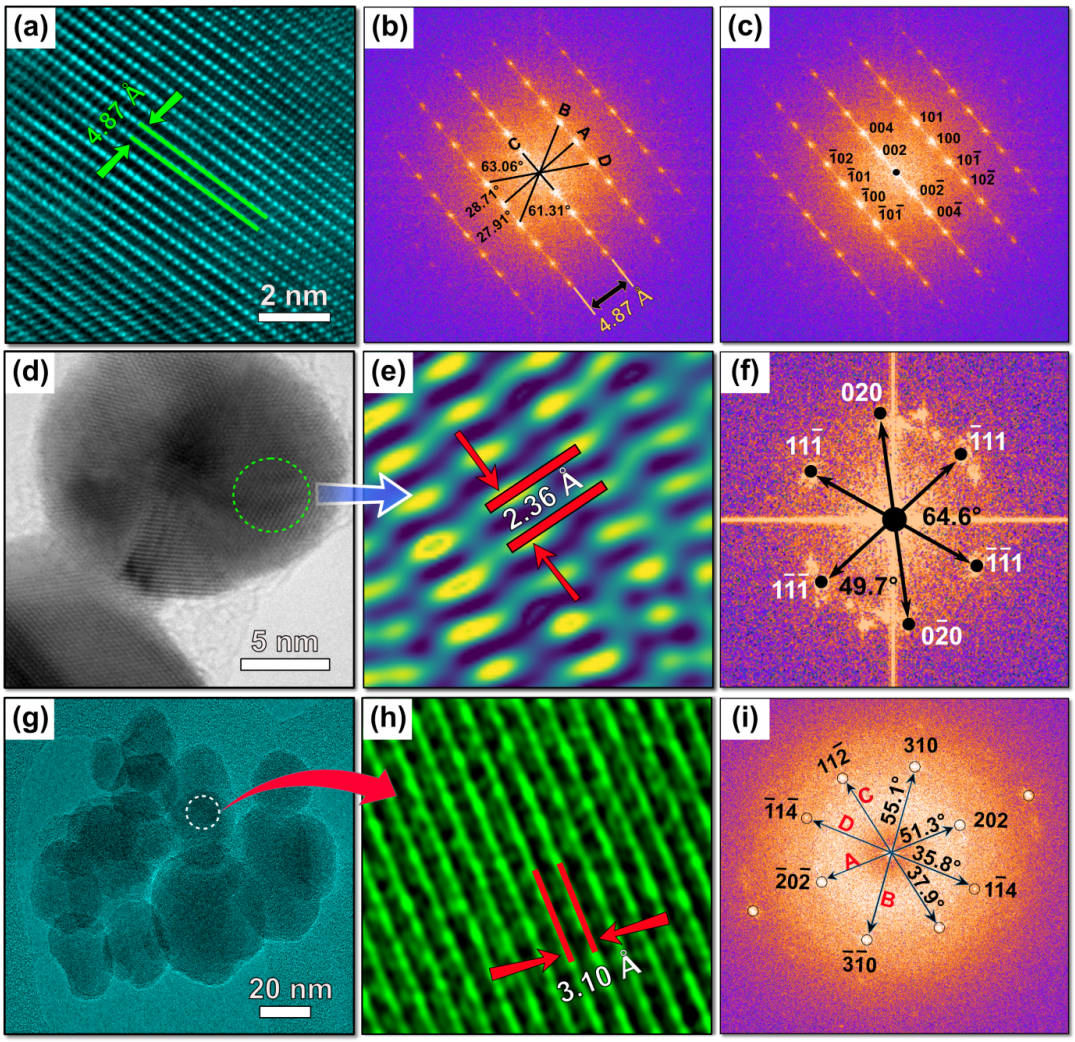

Fig. S8. Lattice fringe 'fingerprinting' of: (a) – (c) single phase GaN crystal; (d) - (e) Ag nanoparticles; and (g) – (i) synthetic magnetite. The images (b) and (c), (f) and (i) are power spectra calculated from the HRTEM micrographs (a), (d) and (g), respectively. GaN crystal: Zone axis = ⟨010⟩; A = 3.4947, B = 4.007, C = 1.8804, D = 3.9289 nm^{-1}; Quality of fit: d-spacing STDEV from GaN crystal (space group $P6_3mc$) = 0.0018. Ag-nanoparticles: Zone axis = ⟨101⟩; A = B = 4.240, C = 4.895 nm^{-1}; d-spacing STDEV from Ag crystal (space group $Fm\bar{3}m$) = 0.0035. Magnetite-nanoparticles: Zone axis = ⟨$\bar{1}$31⟩; A = 3.248, B = 3.801, C =3.090, D = 5.075 nm^{-1}; *d*-spacing STDEV from magnetite crystal (space group $Fd\bar{3}m$) = 0.0107.

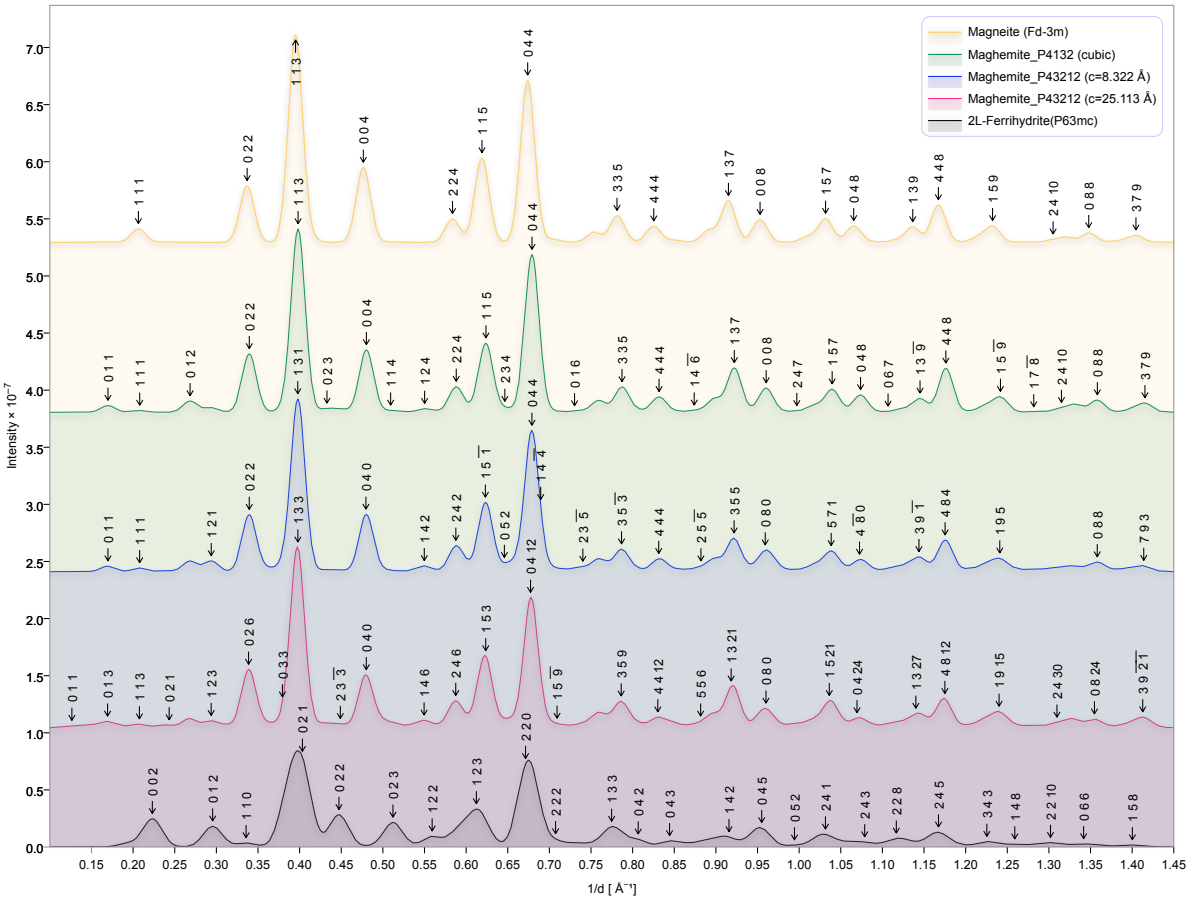

Fig. S9. Comparison between electron diffraction from ideal structures of tetragonal maghemite ($P4_32_12$; c=25.113 Å (14) *and* c=8.322 Å (20)), cubic maghemite ($P4_132$; c=8.330 Å(21)), magnetite ($Fd\bar{3}m$; c=8.394 Å (22)) and 2L-ferrihydrite ($P6_3mc$ (23)). Calculations assume TEM beam voltage of 300 keV, Pseudo-Voigt peak profile and a particle size of 50 nm.

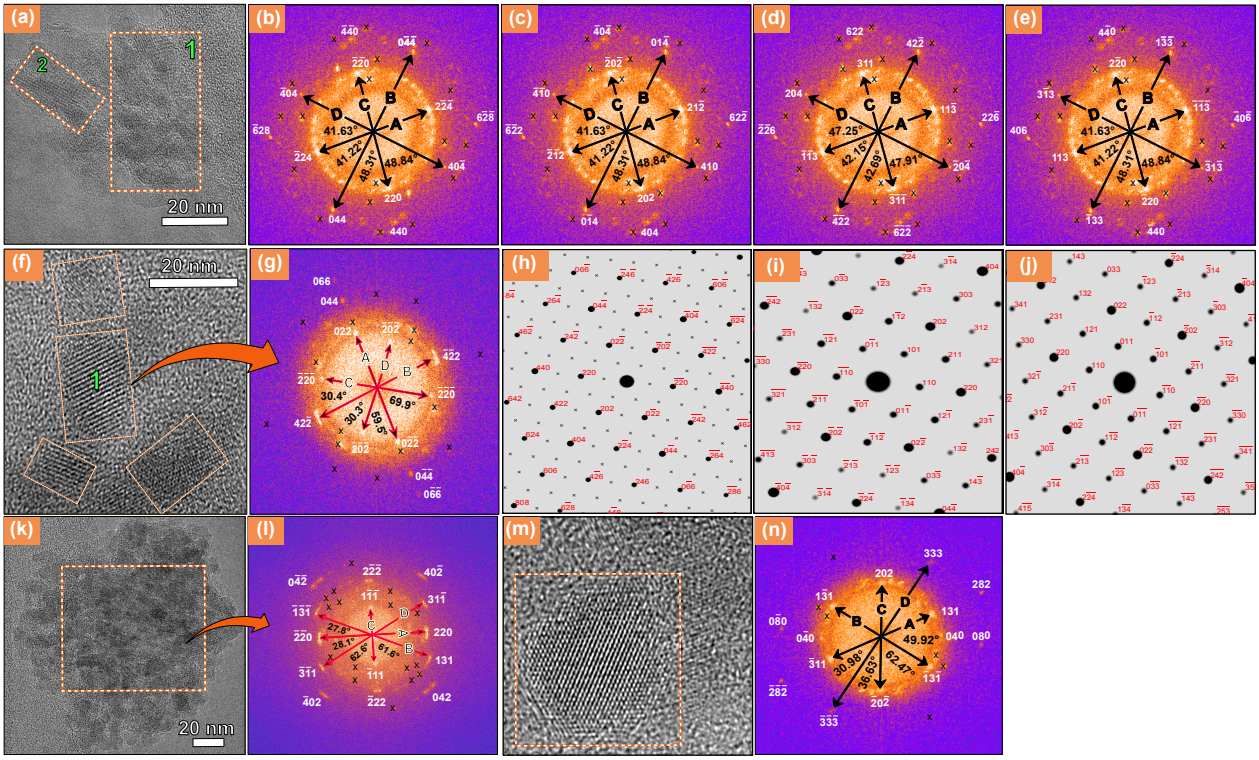

Fig. S10. Examples demonstrating the application of the structural 'fingerprinting' approach. (a) HRTEM of 'old' S_1, Luochuan, CLP paleosol (collected 1990, stored in air for 27 years) and the corresponding FFT power spectra and lattice indexing of (b) a multi-grain area along the tetragonal maghemite ($P4_32_12$; c = 25.113 Å) along zone-axis $\langle 1\bar{1}1\rangle$ (A = 3.775, B = 5.057, C =3.333, D = 5.013 nm^{-1}; σ_d = 0.0026); (c) tetragonal maghemite ($P4_32_12$; c = 8.322 Å) along zone-axis $\langle \bar{1}41\rangle$ (A = 3.775, B = 5.057, C =3.333, D = 5.013 nm^{-1}; σ_d = 0.0065); (d) primitive cubic maghemite ($P4_132$; c = 8.33 Å) along zone-axis $\langle \bar{2}51\rangle$ (A = 3.834, B = 5.635, C =3.797, D = 5.146 nm^{-1}; σ_d = 0.0013) and (e) magnetite ($Fd\bar{3}m$) $\langle \bar{3}\bar{3}2\rangle$ (A = 3.775, B = 5.057, C =3.333, D = 5.013 nm^{-1}; σ_d = 0.0032). (f) HRTEM of 'New' paleosol S_1, CLP sample, (g) the corresponding FFT spectrum and lattice indexing of single grain crystal along the magnetite (best fit) zone-axis $\langle 1\bar{1}1\rangle$ (A = 3.410, B = 3.450, C =3.408, D = 5.881 nm^{-1}; σ_d = 0.0020) and (h) simulated HRTEM diffraction along zone-axis $\langle 1\bar{1}1\rangle$ of (h) magnetite ($Fd\bar{3}m$), (i) tetragonal maghemite ($P4_32_12$; c

= 8.322 Å) and (j) cubic maghemite ($P4_132$; c = 8.33 Å). Note the absence of the (110) and related reflections in experimental FFT that are expected for maghemite but not magnetite. (k) HRTEM of modern Exmoor cambisol and (l) the corresponding FFT spectrum and lattice indexing of multi-grain crystals along the magnetite zone-axis $\langle 1\bar{1}2 \rangle$ (A = 3.447, B = 3.941, C =2.074, D = 4.103 nm^{-1}; σ_d = 0.0039). (m) HRTEM of Lingtai Red Clay sample and (n) the corresponding FFT spectrum and lattice indexing of a single grain crystal along the magnetite zone-axis $\langle \bar{1}01 \rangle$ (A = 3.645, B = 3.801, C =3.148, D = 5.651 nm^{-1}; σ_d = 0.0042). The black '×' symbols represent overlain lattices that have been fitted to the same candidate phase but details removed for clarity. Note that the modulus of the lattice vectors A, B, C and D are represented by half the lengths of the centred arrows in the FFT images.

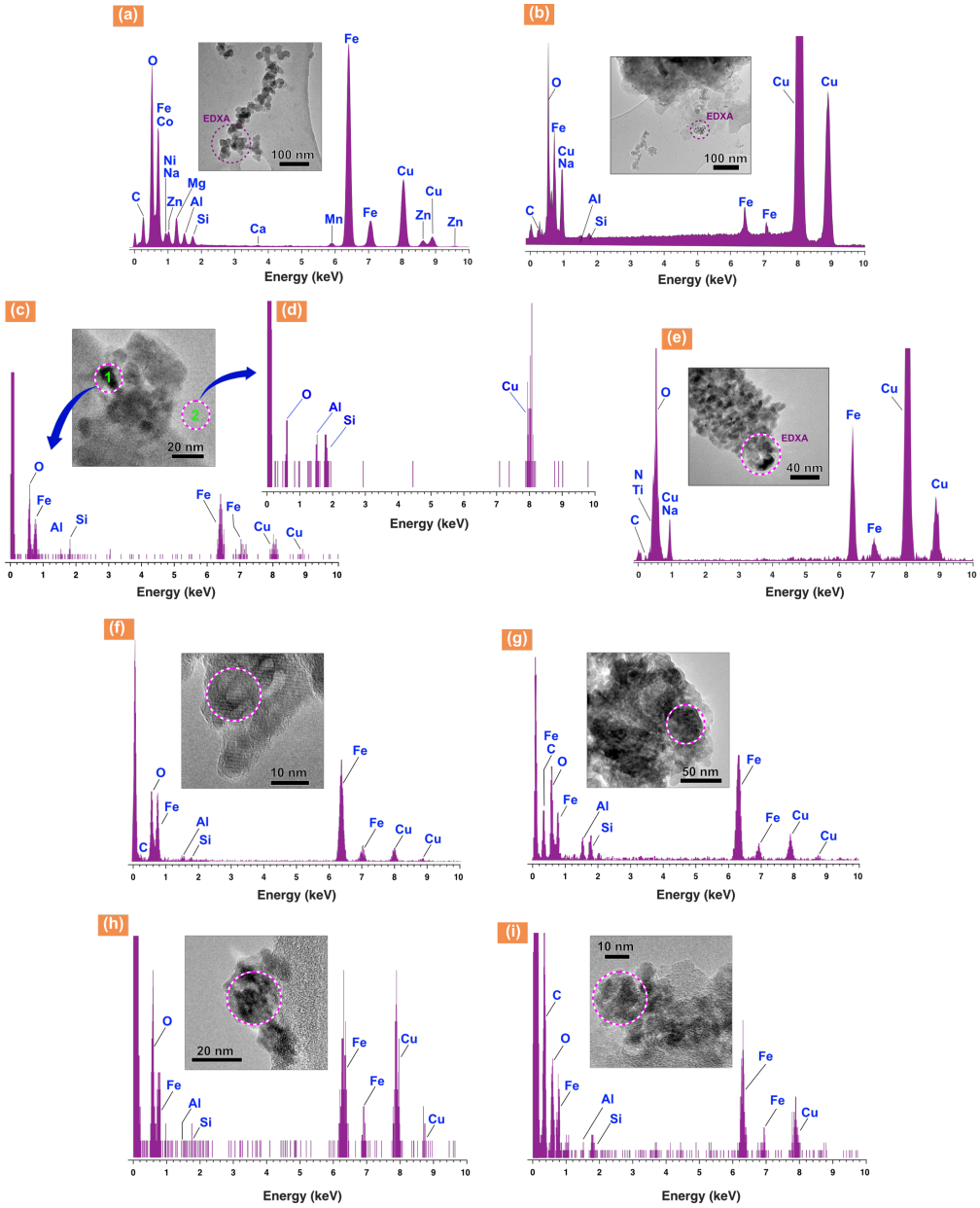

Fig. S11. Energy-dispersive X-ray spectroscopy analysis (EDXA) data and HRTEM from magnetic extracts of (a) and (b): S_1, Luochuan paleosol ('old' CLP sample); (c) – (e): S_1, Luochuan paleosol ('new' CLP sample); (f) and (g): modern Exmoor cambisol; and (h) and (i): Tertiary Red Clay. All the magnetic particles display vanishingly low Al content. Where, in some extracts, the magnetic particles are associated with clay minerals, Si and Al co-occur; in contrast, the Fe-rich particles are notably deficient in Al and Si (e.g., compare (c) with (d)).

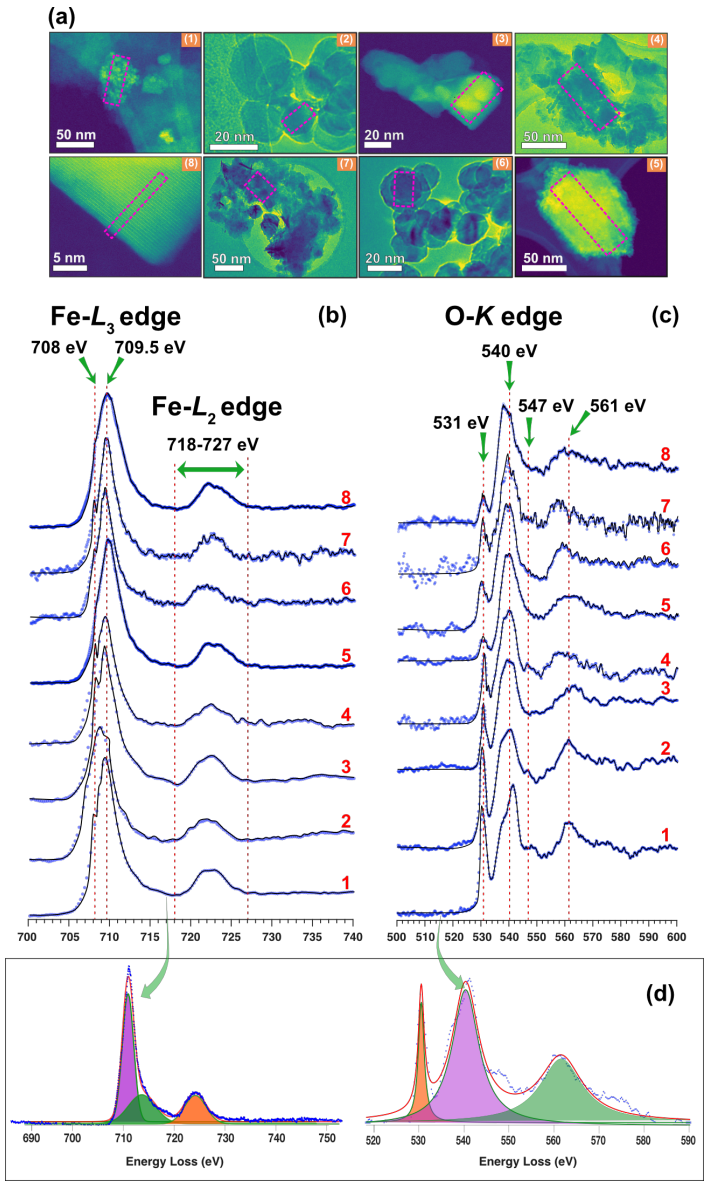

Fig. S12. EELS spectra of paleosol magnetic nanoparticles (a) Scanning TEM micrographs from 'old' (1-4) and 'new' (5-8) paleosol S_1, CLP samples with selected areas corresponding to the resulting EELS spectra. (b) Oxygen-*K* edge and (c) and Fe-$L_{2,3}$ edge after background subtraction of nanoparticles identified in the selected areas in (a). The solid lines in (b) and (c) represent first model fits of experimental data for O-*K* or Fe-$L_{2,3}$. (d) Deconvolution of EELS spectra b1 and c1 showing Gaussian or Lorentzian functions fitted to dominant peaks for determination of their centre, area and FWHM.

References

1. Maher BA (1998) Magnetic properties of modern soil and Quaternary loessic paleosols. Paleoclimatic implications. *Palaeogeography, Palaeoclimatology, Palaeoecology* 137(1-2):25–54.

2. Petersen N, Dobeneck von T, Vali H (1986) Fossil bacterial magnetite in deep-sea sediments from the South Atlantic Ocean. *Nature* 320(6063):611–615.

3. Hounslow MW, Maher BA (1996) Quantitative extraction and analysis of carriers of magnetisation in sediments. *Geophysical Journal International* 124(1):57–74.

4. Hounslow M, Maher B (1999) *Laboratory procedures for quantitative extraction and analysis of magnetic minerals from sediments.*

5. Maher BA (1988) Magnetic properties of some synthetic sub-micron magnetites. *Geophysical Journal* 94(1):83–96.

6. Özdemir Ö, Banerjee SK (1982) A preliminary magnetic study of soil samples from west-central Minnesota. *Earth and Planetary Science Letters* 59(2):393–403.

7. Sawatzky GA, van der Woude F, Morrish AH (1969) Recoilless-Fraction Ratios for Fe^{57} in Octahedral and Tetrahedral Sites of a Spinel and a Garnet. *Physical Review* 183(2):383–386.

8. van der Woude F, Sawatzky GA, Morrish AH (1968) Relation between the Hyperfine Magnetic Fields and Sublattice Magnetizations in Fe3O4. *Physical Review* 167(2):533–535.

9. Sawatzky GA, Coey JMD, Morrish AH (1969) Mössbauer Study of Electron Hopping in the Octahedral Sites of Fe_3O_4. *arXiv* 40(3):1402–1403.

10. Coey JMD, Morrish AH, Sawatzky GA (1971) a Mössbauer study of conduction in magnetite. *J Phys Colloques* 32(C1):C1–271–C1–273.

11. Hägg G (1935) Die Kristallstruktur des magnetischen Ferrioxyds, γ-Fe2O3. *Zeitschrift für Physikalische Chemie* 29B(1). doi:10.1515/zpch-1935-2908.

12. Verwey EJW (1935) The Crystal Structure of γ-Fe2O3 and γ-Al2O3. *Zeitschrift f?r Kristallographie - Crystalline Materials* 91(1-6). doi:10.1524/zkri.1935.91.1.65.

13. Braun PB (1952) A Superstructure in Spinels. *Nature* 170(4339):1123–1123.

14. Jørgensen J-E, Mosegaard L, Thomsen LE, Jensen TR, Hanson JC (2007) Formation of γ-Fe_2O_3 nanoparticles and vacancy ordering: An in situ X-ray powder diffraction study. *Journal of Solid State Chemistry* 180(1):180–185.

15. Greaves C (1983) A powder neutron-diffraction investigation of vacancy vrdering and covalence in gamma-Fe_2O_3. *Journal of Solid State Chemistry* 49(3):325–333.

16. Grau-Crespo R, Al-Baitai AY, Saadoune I, de Leeuw NH (2010) Vacancy ordering and electronic structure of γ -Fe 2O 3(maghemite): a theoretical investigation. *J Phys: Condens Matter* 22(25):255401–8.

17. Collyer S, Grimes NW, Vaughan DJ (2000) Does magnetite lack a centre of symmetry? *Journal of Physics C: Solid State Physics* 21(29):L989–L992.

18. Kelm K, Mader W (2006) The symmetry of ordered cubic gamma-Fe2O3 investigated by TEM. *Zeitschrift Fur Naturforschung Section B-a Journal of Chemical Sciences* 61(6):665–671.

19. Schneider CA, Rasband WS, Eliceiri KW (2012) NIH Image to ImageJ: 25 years of image analysis. *Nat Methods* 9(7):671–675.

20. Greaves GN (1983) A powder neutron diffraction investigation of vacancy ordering and covalence in γ-Fe2O3. *Journal of Solid State Chemistry* 49(3):325–333.

21. Pecharroman C, Gonzalezcarreno T, Iglesias JE (1995) The Infrared Dielectric-Properties of Maghemite, Gamma-Fe2o3, From Reflectance Measurement on Pressed Powders. *Physics and Chemistry of Minerals* 22(1):21–29.

22. Fleet ME (1981) The structure of magnetite. *Acta Crystallographica Section B Structural Crystallography and Crystal Chemistry* 37(4):917–920.

23. Michel FM, et al. (2007) The structure of ferrihydrite, a nanocrystalline material. *Science* 316(5832):1726–1729.

24. Spassov S (2002) Loess magnetism, environment and climate change on the Chinese Loess Plateau. Dissertation (ETH, Zürich, Switzerland. Thesis no. 14976., Zürich, Switzerland).

25. Maher BA (2016) Palaeoclimatic records of the loess/palaeosol sequences of the Chinese Loess Plateau. *Quaternary Science Reviews* 154(C):23–84.